lubricants

Article

Combined Effect of Fluid Cavitation and Inertia on the Pressure Buildup of Parallel Textured Surfaces

Xuezhong Ma

College of Petrochemical Engineering, Lanzhou University of Technology, Lanzhou 730050, China; maxz@lut.edu.cn

Abstract: A mathematical model is developed to investigate the combined effect of fluid cavitation and inertia on the fluid pressure buildup of parallel textured surfaces. The fluid cavitation is analyzed using the Rayleigh–Plesset model, and the fluid inertia is analyzed with an averaged method. The finite element method and Newton-downhill method are employed to solve the governing equations. The numerical model is validated by comparing the experimental and numerical results, and the combined effect of fluid cavitation and inertia on the fluid pressure buildup is analyzed and discussed. The research indicates that the cavitation weakens the fluid inertia effect on the pressure distribution at the inlet area of textures. The fluid inertia greatly enhances the hydrodynamic effect and effectively limits the excessive extension of the low-pressure zone caused by cavitation. The fluid cavitation and inertia, especially their interaction, significantly affect the fluid pressure buildup and generate a net load-carrying capacity (LCC). The numerical model with the fluid inertia and cavitation is more time saving than the commercial CFD tools in solutions, which gives a novel and optional HD foundation for developing a more efficient and accurate THD or TEHD model by numerical programming.

Keywords: cavitation; inertia; surface texture; pressure buildup; finite element method

check for updates

Citation: Ma, X. Combined Effect of Fluid Cavitation and Inertia on the Pressure Buildup of Parallel Textured Surfaces. *Lubricants* **2023**, *11*, 270. https://doi.org/10.3390/lubricants11070270

Received: 6 May 2023
Revised: 7 June 2023
Accepted: 17 June 2023
Published: 21 June 2023

1. Introduction

In hydrodynamic lubrication, the fluid cavitation and inertia are two common special effects, especially at the location where the fluid film thickness changes suddenly. The fluid film cavitation is complicated and attracts researchers' attention more often. In the review of fluid film cavitation [1], Braun et al. outlined three recognized forms of fluid cavitation: gaseous cavitation, pseudo-cavitation and vaporous cavitation. Several studies [2–6] have shown that it affects the fluid pressure buildup, so that the fluid film does not appear negative pressure or too low pressure. Studies [7–9] on the fluid inertia of textured surfaces showed that it can significantly affect the fluid pressure buildup due to the side wall. Their effects on the fluid pressure buildup of textured surface have been often investigated separately. In some cases, fluid cavitation and inertia, however, are simultaneously encountered, and they affect the pressure distribution of fluid film together as well as influence each other. Therefore, it is necessary to take into account the above two effects simultaneously for these cases.

Nowadays, the Reynolds equation (RE) combined with JFO boundary conditions (RE-JFO) [10–12] is a widely accepted mass-conserving model in analyzing textured surfaces. Singhal et al. [13] developed a full cavitation model (FCM) and incorporated it into the CFD software. Then, Bakir et al. [14] outlined the volume fraction (VOF) model in the CFD software and analyzed the cavitation behavior in an inducer. The simulation results are in good agreement with the experimental results. Both of the cavitation models above are based on the Rayleigh–Plesset equation (RPE) in the dynamics theory of cavitation bubbles [15]. Remarkably, they satisfy the mass conservation. Compared with the JFO theory, it can better approximate the physical process of fluid cavitation. Several researchers [16–21] have successfully analyzed the hydrodynamic lubrication in journal bearings by the similar cavitation models based on RPE. Recently, Wang et al. [22] presented a homogeneous phase change model by combining the RPE and RE to investigate the boiling flow in wavy face seals. It can be observed that the RPE model is a feasible means to analyze the cavitation flow of fluid film.

To study the fluid inertia effect on the pressure distribution of textured surfaces, several researchers [7,8] have solved the Navier–Stokes equations (NSEs) by the CFD technology. Despite its advantage in the detailed investigation of fluid inertia, the numerical calculation based on NSEs is very time consuming. Another way to deal with fluid inertia is based on the hypothesis proposed by Constantinescu and Galetuse [23]. They assume that fluid inertia only affects the velocity magnitude and does not affect the velocity profile. This method has been successfully used to study the fluid inertia effect on the hydrostatic seals [24], in which the seal face is a two-dimensional axisymmetric structure. In general, it has a better approximation to the fluid inertia for the shallow textures and grooves due to the limitation of the assumption.

The above short review emphasizes the problem in the studies on the fluid cavitation and inertia of textured surfaces as well as their treatments and solutions. Moreover, the research objects are often tribological components with surface texture, such as seals [25,26], bearings [27,28], piston rings [29] and so on. Recesses of various shapes, as ones of the typical surface textures, have been widely used in the above fields. In order to study the mechanism conveniently, the sliding cell shown in Figure 1 is taken as the research object instead of a specific tribological component.

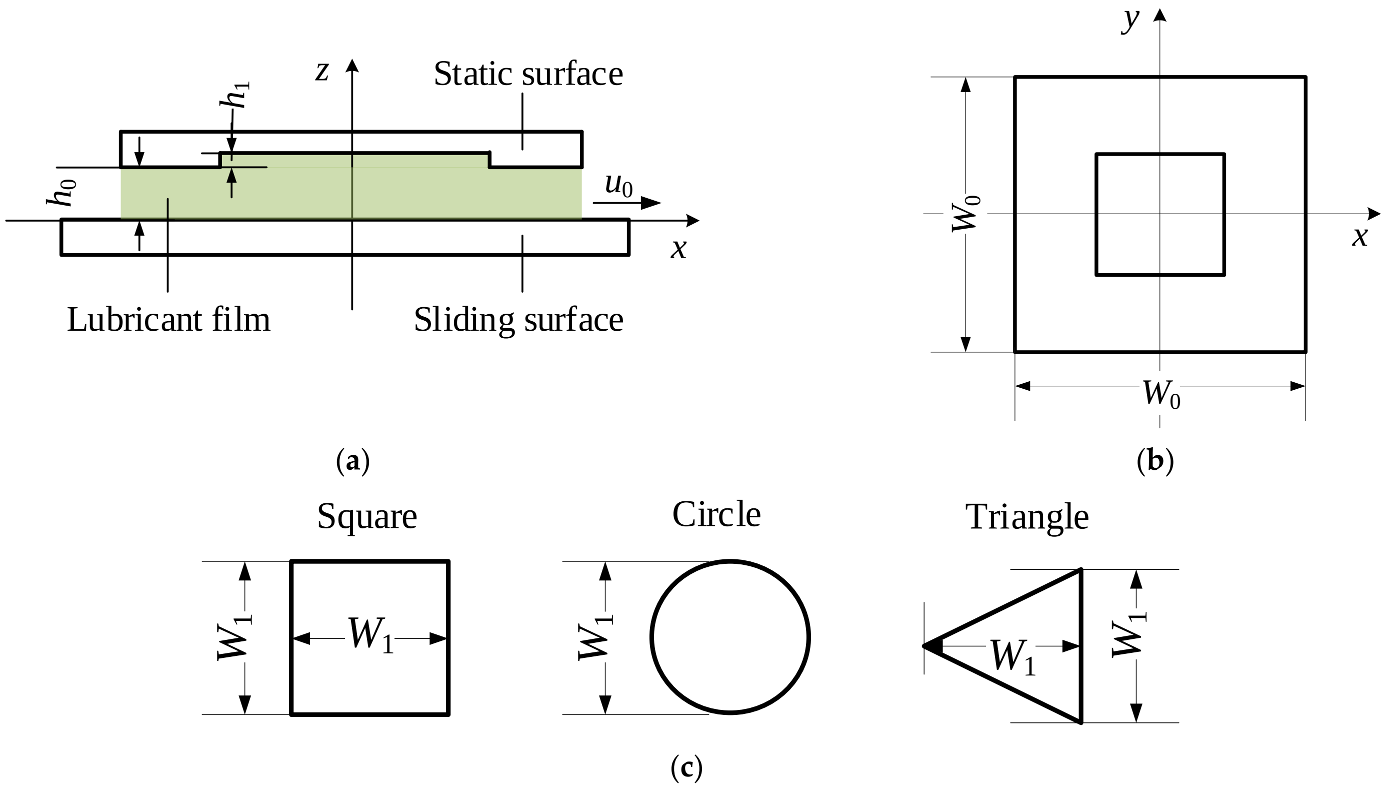

Figure 1. Geometrical model: (**a**) Parallel sliding surfaces, (**b**) Textured surface cell and (**c**) Recess shapes.

In this work, a mathematical model with fluid cavitation and inertia based on the RPE [15] and hypothesis of Constantinescu and Galetuse [23] is proposed for the parallel surfaces with a shallow recess. A numerical procedure is developed to solve the governing equations by the finite element method and Newton-downhill technology. The numerical model is then validated by confronting it with the previously published experimental results and the numerical ones by RE-JFO and CFD. The combined effect of fluid cavitation and inertia on the fluid pressure buildup and their interaction mechanism are analyzed and discussed.

2. Theoretical Models

2.1. Geometrical Model

The geometrical model of the parallel sliding surfaces with a shallow recess is shown in Figure 1a,b. In the model, the lower surface moves along the x direction with a velocity u_0, while the upper surface cell with a side length W_0 is stationary. A shallow recess is located in the center of the upper surface cell, where its shapes include a square, circle, and triangle (shown in Figure 1c), it has the same length W_1 along the x and y directions, and its depth is denoted by h_1. The gap between two surfaces is filled with the lubricant #15 aviation hydraulic oil with the film thickness h_0 in the non-textured area. The film thickness between the parallel surfaces is given as

$$h = \begin{cases} h_0 & \text{non-textured region} \\ h_0 + h_1 & \text{textured region} \end{cases} \tag{1}$$

The geometric and operating parameters used in the paper are listed in Table 1.

Table 1. Geometric parameters and operating parameters.

Parameters	Values
Textured surface cell side length, $W_0/(\text{mm})$	6
Recess size length, $W_1/(\text{mm})$	4
Gap thickness, $h_0/(\mu\text{m})$	50
Recess depth, $h_1/(\mu\text{m})$	4
Ambient pressure, $p_a/(\text{MPa})$	0.1
Cavitation pressure, $p_c/(\text{MPa})$	0.095
Dynamic viscosity of liquid, $\mu_L/(\text{Pa}\cdot\text{s})$	0.0127
Liquid density, $\rho_L/(\text{kg/m}^3)$	840
Reynolds number, Re	165.35

2.2. Mathematical Model

The following assumptions are made in the present model.

1. The roughness of parallel surfaces is neglected, and the slip flow between the surfaces and the fluid film are not considered.
2. The flow regime of the fluid film is laminar, as calculated from Re.
3. The fluid inertia only affects the velocity magnitude and does not affect the velocity profile [23,24].
4. The fluid film in the cavitation zone is a homogeneous mixture of liquid and vapor, and the mixture is assumed to be isothermal and incompressible [14,22,30].
5. The density of liquid is considered constant, the vapor is assumed to be the ideal gas, and the non-condensable gas in the fluid film is not considered. The relative motion between them is neglected and they share the same flow rates and pressure [14,22,30].

2.2.1. Mixture Mass and Momentum Equations

The equation of mass conservation for the steady flow can be expressed as follows.

$$\frac{\partial u}{\partial x} + \frac{\partial v}{\partial y} + \frac{\partial w}{\partial z} = 0 \tag{2}$$

where u, v and w are the velocity components in the x, y and z coordinate systems. Since the film thickness in the z direction is in the micrometer level, much smaller than the scales in the x and y directions, the pressure variation along the film thickness is neglected. The NSEs can be written as

$$\rho\left(u\frac{\partial u}{\partial x}+v\frac{\partial u}{\partial y}+w\frac{\partial u}{\partial z}\right)=-\frac{\partial p}{\partial x}+\mu\frac{\partial^2 u}{\partial z^2} \tag{3}$$

$$\rho\left(u\frac{\partial v}{\partial x}+v\frac{\partial v}{\partial y}+w\frac{\partial v}{\partial z}\right)=-\frac{\partial p}{\partial y}+\mu\frac{\partial^2 v}{\partial z^2} \tag{4}$$

$$0=\frac{\partial p}{\partial z} \tag{5}$$

where p, ρ and μ are the pressure, density and dynamic viscosity of the mixture, respectively. The physical property parameters ρ and μ of the mixture are to be defined in Section 2.2.2. Equations (3) and (4) are rewritten in the following forms based on the mass conservation shown in Equation (2).

$$\rho\left(\frac{\partial u^2}{\partial x}+\frac{\partial vu}{\partial y}+\frac{\partial wu}{\partial z}\right)=-\frac{\partial p}{\partial x}+\mu\frac{\partial^2 u}{\partial z^2} \tag{6}$$

$$\rho\left(\frac{\partial uv}{\partial x}+\frac{\partial v^2}{\partial y}+\frac{\partial wv}{\partial z}\right)=-\frac{\partial p}{\partial y}+\mu\frac{\partial^2 v}{\partial z^2} \tag{7}$$

Integrating Equations (2), (6) and (7) in the z direction, where the following forms can be obtained (note that the velocity component w along the z axis is 0),

$$\frac{\partial}{\partial x}\int_0^h udz+\frac{\partial}{\partial y}\int_0^h vdz=0 \tag{8}$$

$$\rho\left(\frac{\partial}{\partial x}\int_0^h u^2dz+\frac{\partial}{\partial y}\int_0^h uvdz\right)=-\frac{\partial p}{\partial x}h+\left(\mu\frac{\partial u}{\partial z}\right)\Big|_0^h \tag{9}$$

$$\rho\left(\frac{\partial}{\partial x}\int_0^h uvdz+\frac{\partial}{\partial y}\int_0^h v^2dz\right)=-\frac{\partial p}{\partial y}h+\left(\mu\frac{\partial v}{\partial z}\right)\Big|_0^h \tag{10}$$

According to Refs. [23,24], the velocity profiles of inertial flow can be deduced as

$$\begin{cases} u=\left(\frac{6q_x}{h^2}z+u_0\right)\left(1-\frac{z}{h}\right) \\ v=\frac{6q_y}{h^2}z\left(1-\frac{z}{h}\right) \end{cases} \tag{11}$$

The variables q_x and q_y are the flow rates of unit length along the x and y directions. Introducing Equation (11) into Equations (8)–(10) gives

$$\frac{\partial q_x}{\partial x}+\frac{\partial q_y}{\partial y}+\frac{u_0}{2}\frac{\partial h}{\partial x}=0 \tag{12}$$

$$\rho\left(\frac{\partial I_{xx}}{\partial x}+\frac{\partial I_{xy}}{\partial y}\right)+h\frac{\partial p}{\partial x}+\frac{12\mu}{h^2}q_x=0 \tag{13}$$

$$\rho\left(\frac{\partial I_{xy}}{\partial x}+\frac{\partial I_{yy}}{\partial y}\right)+h\frac{\partial p}{\partial y}+\frac{12\mu}{h^2}q_y=0 \tag{14}$$

where I_{xx}, I_{xy}, and I_{yy} are the integrals of the products of velocity components along the z direction, which are defined as follows.

$$I_{xx}=\int_0^h u^2dz=\frac{6}{5h}q_x^2+q_xu_0+\frac{1}{3}hu_0^2 \tag{15}$$

$$I_{xy} = \int_0^h uvdz = \frac{6}{5h} q_x q_y + \frac{1}{2} q_y u_0 \tag{16}$$

$$I_{yy} = \int_0^h v^2 dz = \frac{6}{5h} q_y^2 \tag{17}$$

2.2.2. Mass Transfer Equations

According to the theory of homogeneous two-phase flow [22,30], the physical property parameters ρ and μ of the mixture are defined as follows.

$$\rho = F_L \rho_L + F_G \rho_G \tag{18}$$

$$\mu = F_L \mu_L + F_G \mu_G \tag{19}$$

where ρ_L and ρ_G are the densities of the liquid and vapor, ρ_L is constant and ρ_G is given by the ideal gas state equation. F_L and F_G are the volume fractions of the liquid and vapor per unit volume in the mixture, which can be defined as

$$\begin{cases} F_L = \frac{V_L}{V_L + V_G} \\ F_G = \frac{V_G}{V_L + V_G} \end{cases} \tag{20}$$

where V_L and V_G are liquid and vapor volumes, respectively.

The liquid flow and vapor flow are governed by the following split phase mass transfer equations:

$$\begin{cases} \frac{\partial}{\partial x}(F_L \rho_L u) + \frac{\partial}{\partial y}(F_L \rho_L v) + \frac{\partial}{\partial z}(F_L \rho_L w) = S \\ \frac{\partial}{\partial x}(F_G \rho_G u) + \frac{\partial}{\partial y}(F_G \rho_G v) + \frac{\partial}{\partial z}(F_G \rho_G w) = -S \end{cases} \tag{21}$$

where S is the cavitation source term and is defined in Section 2.2.3. According to the assumption (5) and Section 2.2.1, the w value is 0. Integrating Equation (21) along the film thickness direction (z axis), the integral forms can be expressed as

$$\begin{cases} \frac{\partial}{\partial x}\left(F_L \rho_L \int_0^h udz\right) + \frac{\partial}{\partial y}\left(F_L \rho_L \int_0^h vdz\right) = Sh \\ \frac{\partial}{\partial x}\left(F_G \rho_G \int_0^h udz\right) + \frac{\partial}{\partial y}\left(F_G \rho_G \int_0^h vdz\right) = -Sh \end{cases} \tag{22}$$

The integral forms of the mixture velocity components in Equation (11) across the film thickness are as follows

$$\begin{cases} \int_0^h udz = \int_0^h \left(\frac{6q_x}{h^2} z + u_0\right)\left(1 - \frac{z}{h}\right)dz = q_x + \frac{u_0 h}{2} \\ \int_0^h vdz = \int_0^h \frac{6q_y}{h^2} z\left(1 - \frac{z}{h}\right)dz = q_y \end{cases} \tag{23}$$

Introducing Equation (23) into Equation (22), we can obtain

$$\begin{cases} \frac{\partial}{\partial x}\left(F_L \rho_L \left(q_x + \frac{u_0 h}{2}\right)\right) + \frac{\partial}{\partial y}(F_L \rho_L q_y) = Sh \\ \frac{\partial}{\partial x}\left(F_G \rho_G \left(q_x + \frac{u_0 h}{2}\right)\right) + \frac{\partial}{\partial y}(F_G \rho_G q_y) = -Sh \end{cases} \tag{24}$$

Equation (24) can be rewritten as

$$\frac{\partial F_L}{\partial x}\left(q_x + \frac{u_0 h}{2}\right) + \frac{\partial F_L}{\partial y} q_y - \frac{(1 - F_L)F_L}{p}\left(\frac{\partial p}{\partial x}\left(q_x + \frac{u_0 h}{2}\right) + \frac{\partial p}{\partial y} q_y\right) - \left(\frac{(1 - F_L)}{\rho_L} + \frac{F_L}{\rho_G}\right) Sh = 0 \tag{25}$$

where there is only one unknown variable F_L, because F_G is replaced by $1 - F_L$.

2.2.3. Cavitation Source Term: RPE Model

The RPE in the dynamics theory of cavitation bubbles [15] can well describe the growth and rupture of cavitation bubbles. Without considering the effects of viscous damping and surface tension, the first-order approximation of RPE [13–15] can be written as

$$ {}_{b} = \sqrt{\frac{2}{3}\frac{|p - p_c|}{\rho_L}} \tag{26}$$

where p_c is the cavitation pressure of the fluid film, and $\acute{R}_b$ is the dynamic radius of cavitation bubbles. It is assumed that bubbles grow from an initial average radius of R_b when the liquid film ruptures and the bubbles change to the initial ones when the liquid film regenerates. The initial average radius R_b can be assumed to be 1 μm [14]. When the liquid film ruptures and regenerates, cavitation source terms can be written as

$$ S = \begin{cases} -C_1 N \rho_G 4\pi R_b^2 |{}_b| & p < p_c \\ C_2 N \rho_G 4\pi R_b^2 |{}_b| & p > p_c \end{cases} \tag{27}$$

where C_1 and C_2 are the empirical coefficients of vaporization and liquefaction, respectively. The values provided in Ref. [22] are used.

$$ C_1 = C_2 = 0.05\frac{|p - p_c|}{p_c} \tag{28}$$

N is the number of initial bubbles per unit volume in the mixture. It has been given as follows in Ref. [14].

$$ N = \begin{cases} \frac{3F_L}{4\pi R_b^3} & p < p_c \\ \frac{3F_G}{4\pi R_b^3} & p > p_c \end{cases} \tag{29}$$

Then, the source term in Equation (27) can be written uniformly as

$$ S = T\rho_G 4\pi R_b^2 \sqrt{\frac{2}{3}\frac{|p - p_c|}{\rho_L}}\,\mathrm{sgn}(p - p_c) \tag{30}$$

where T is a comprehensive coefficient, and it makes vaporization and liquefaction source terms to be a unified formula.

$$ T = 0.05\frac{|p - p_c|}{p_c}\left(\frac{-(p - p_c) + |p - p_c|}{2p_c}\frac{3F_L}{4\pi R_b^3} + \frac{(p - p_c) + |p - p_c|}{2p_c}\frac{3(1 - F_L)}{4\pi R_b^3}\right) \tag{31}$$

Equation (31) has already been presented in Ref. [22] and applied directly in the present model.

2.2.4. Boundary Conditions

The governing equations of the present model include Equations (12)–(14) and Equation (25). The unknown variables include p, q_x, q_y and F_L. To solve the governing equations, the periodic boundary conditions shown in Equation (32) and the imposed boundary conditions shown in Equation (33) are employed.

$$ q_x(x = -3) = q_x(x = 3) \tag{32a}$$

$$ q_y(x = -3) = -q_y(x = 3) \tag{32b}$$

$$ p(x = -3) = p(x = 3) \tag{32c}$$

$$F_L(x=-3) = F_L(x=3) \tag{32d}$$

$$p(y=-3) = p(y=3) = p_a \tag{33a}$$

$$F_L(y=-3) = F_L(y=3) = 1 \tag{33b}$$

3. Numerical Procedure

The numerical model is solved by the numerical programming with the finite element method. The Newton-downhill method is applied to solve the nonlinear Equations (12)–(14) and (25). The weighted residual forms of governing equations are as follows.

$$Rc_i = \int_\Omega w_i\left(\frac{\partial q_x}{\partial x} + \frac{\partial q_y}{\partial y} + \frac{u_0}{2}\frac{\partial h}{\partial x}\right)dxdy \tag{34}$$

$$Rmx_i = \int_\Omega w_i\left(\rho\left(\frac{\partial I_{xx}}{\partial x} + \frac{\partial I_{xy}}{\partial y}\right) + h\frac{\partial p}{\partial x} + \frac{12\mu}{h^2}q_x\right)dxdy \tag{35}$$

$$Rmy_i = \int_\Omega w_i\left(\rho\left(\frac{\partial I_{xy}}{\partial x} + \frac{\partial I_{yy}}{\partial y}\right) + h\frac{\partial p}{\partial y} + \frac{12\mu}{h^2}q_y\right)dxdy \tag{36}$$

$$RF_{Li} = \int_\Omega w_i\left(\frac{\partial F_L}{\partial x}\left(q_x + \frac{u_0 h}{2}\right) + \frac{\partial F_L}{\partial y}q_y - \frac{(1-F_L)F_L}{p}\left(\frac{\partial p}{\partial x}\left(q_x + \frac{u_0 h}{2}\right) + \frac{\partial p}{\partial y}q_y\right) - \left(\frac{(1-F_L)}{\rho_L} + \frac{F_L}{\rho_G}\right)Sh\right)dxdy \tag{37}$$

where w_i is a weight function on the two-dimensional computational domain Ω. When the numerical solution converges, the above residuals tend to zero. Numerical iterative systems with the Newton-downhill method are as follows.

$$-\begin{bmatrix} \frac{\partial Rmx_i}{\partial q_{xj}} & \frac{\partial Rmx_i}{\partial q_{yj}} & \frac{\partial Rmx_i}{\partial p_j} \\ \frac{\partial Rmy_i}{\partial q_{xj}} & \frac{\partial Rmy_i}{\partial q_{yj}} & \frac{\partial Rmy_i}{\partial p_j} \\ \frac{\partial Rc_i}{\partial q_{xj}} & \frac{\partial Rc_i}{\partial q_{yj}} & 0 \end{bmatrix}\begin{bmatrix} \delta q_{xj} \\ \delta q_{yj} \\ \delta p_j \end{bmatrix} = \lambda_{qp}\begin{bmatrix} Rmx_i \\ Rmy_i \\ Rc_i \end{bmatrix} \tag{38}$$

$$-\left[\frac{\partial RF_{Li}}{\partial F_{Lj}}\right][\delta F_{Lj}] = \lambda_F[RF_{Li}] \tag{39}$$

Then, the variables are expressed as

$$\begin{cases} q_x^{(k)} = q_x^{(k-1)} + \delta q_x^{(k)} \\ q_y^{(k)} = q_y^{(k-1)} + \delta q_y^{(k)} \\ p^{(k)} = p^{(k-1)} + \delta p^{(k)} \end{cases} \tag{40}$$

$$F_L^{(k)} = F_L^{(k-1)} + \delta F_L^{(k)} \tag{41}$$

where k is the number of iterations. The procedure convergence criterion is as follows, where X includes p, q_x, q_y and F_L.

$$\sum\left|\frac{X^{(k)} - X^{(k-1)}}{X^{(k)}}\right| < 10^{-4} \tag{42}$$

The LCC and flow rate can be expressed as

$$F_o = \int_{\Omega} p dx dy \tag{43}$$

$$Q = \int_{l} (q_x l_x + q_y l_y) dl \tag{44}$$

where l is the integral curve, and l_x and l_y are the unit vectors along the x and y directions.

The numerical procedure is described as follows.

(1). Input geometric and operating parameters.
(2). Give initial values $X^{(0)}$ ($p^{(0)}$, ${q_x}^{(0)}$, ${q_y}^{(0)}$, ${F_L}^{(0)}$) to unknown variables X (p, q_x, q_y, F_L), and impose pre-boundary conditions.
(3). Calculate the physical property parameters ρ, μ and flow characteristic parameters I_{xx}, I_{xy}, and I_{yy}.
(4). Solve Equation (38) and obtain the pressure and flow rate distributions.
(5). Solve Equation (39) based on step (4) and obtain the liquid volume fraction distribution.
(6). Check the convergence criterion. If the unknowns meet the tolerance, end the iteration; otherwise, go to step (3) and repeat the procedure.
(7). Output results and post-processing.

4. Results and Discussion

4.1. Validation

To validate the mathematical model and computational procedure, the results given by the present model are compared with the published experimental results of the journal bearing in Ref. [31]. They are further compared with the numerical results from the RE-JFO model, which is solved with the method in Ref. [32]. Figure 2 shows the pressure profiles at the centerline of the journal bearing. It shows that the pressure peak from the present model is higher than that from the RE-JFO model. This may be the effect of the fluid inertia. The cavitation zone obtained from the present model is narrower than that from the RE-JFO model. It seems that the pressure distribution from the present model is more consistent with the experimental results than the RE-JFO model. In order to further verify the cavitation prediction of textured surfaces, Figure 3 shows the pressure distribution of the circle recess with a side length W_1 = 3 mm at a very small Re = 0.265 and a small gap thickness h_0 = 10 µm, where the Reynolds number Re is defined as $\rho_L u_0 h_0 / \mu_L$. It is worth noting that the pressure in the low-pressure zone given by the present model changes continuously near the cavitation pressure p_c (0.08 MPa) rather than the fixed value. The main reason is that in the present model, the p_c is only used to calculate the source term S, and the pressure in the cavitation region is solved by the mass conservation equation and momentum equations. It is in accordance to many experimental research papers on cavitation [1,33]. In addition, according to the Bernoulli equation, when the fluid flows through the recess, the pressure should first decrease and then increase. Although the fluid cavitation makes the pressure in the cavitation region greatly increase, its trend should be consistent. In general, the pressure distribution given by the present model is in good agreement with the one given by the RE-JFO model. The above verification analysis shows that the present model can well solve the cavitation problem of textured surfaces.

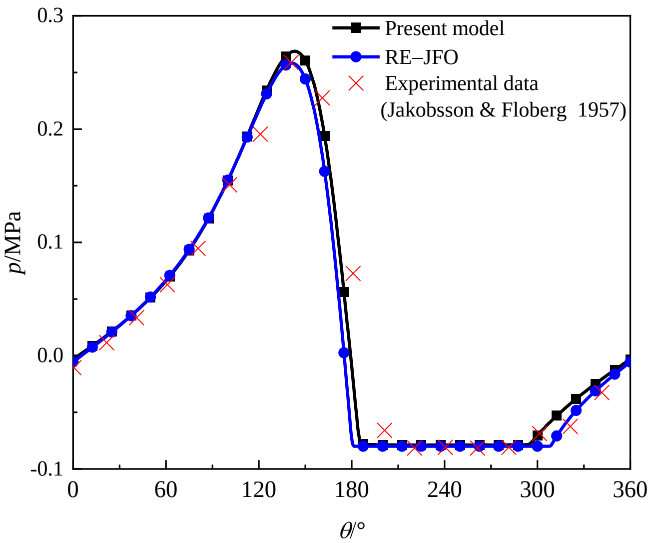

Figure 2. Pressure distribution of the journal bearing [31].

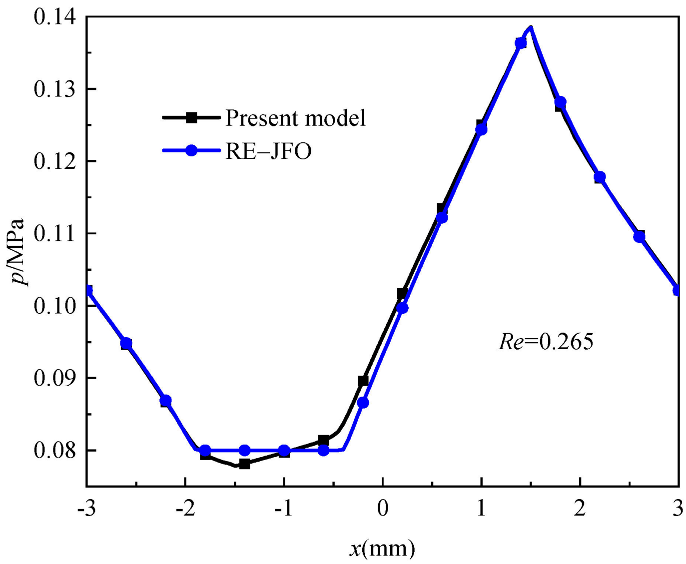

Figure 3. Pressure distribution of the circle recess.

Figure 4 shows the fluid pressure distribution of the square recess with a side length W_1 = 3 mm at y = 0 when the fluid cavitation is neglected for the case of Re = 148.82. The pressure distribution from the present model is compared with the results by solving N-S equations from ANSYS FLUENT (NSEs) and by solving the Reynolds equation (RE). Due to the change of fluid film thickness, a low-pressure zone is generated around the zone of $x = -1.5$, and a high one is generated around the zone of x = 1.5. When the fluid inertia is not considered, that is the result from the RE, and the fluid pressure distribution shows triangular profiles. For the case of NSEs and the present model, there are pressure jumps at $x = -1.5$ and x = 1.5 due to the fluid inertia. The pressure peak values are larger and valley values are smaller than those from the RE. That means the fluid inertia plays a remarkable role in the fluid pressure distribution. It is worth noting that the results from the present model and the NSEs agree well with each other. It proves that the present model is validated.

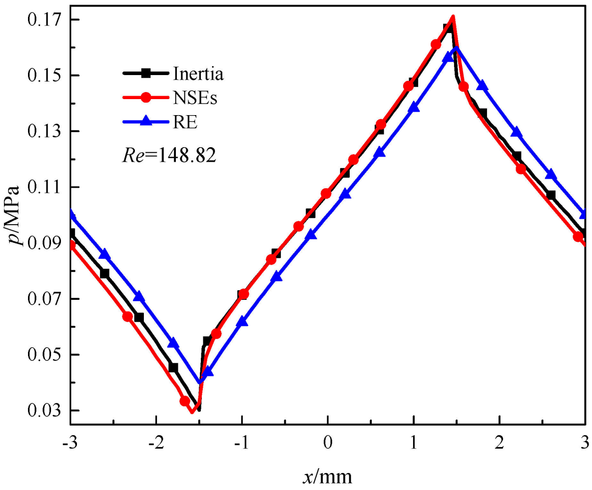

Figure 4. Pressure distribution of the square recess.

In this paper, the triangular elements are used to discretize the computational domain. The meshes in the recess region are denser than those in the other region because the cavitation may occur there (shown in Figure 5a). The mesh independence of the present model is checked, and the results are shown in Figure 5b. It indicates that with the increase in the node number, the LCC of the fluid film and the flow rates on the periodic boundaries gradually tend to their stable values.

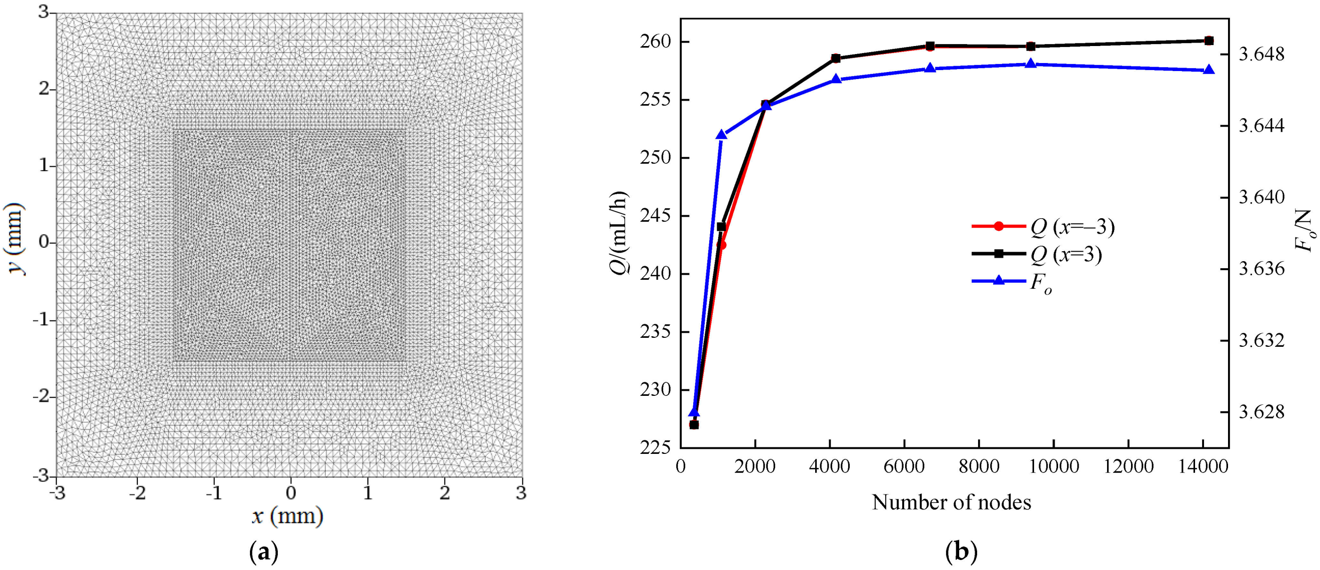

Figure 5. (**a**) Mesh and (**b**) Validation of mesh independence.

4.2. Effect of *Re*

Figure 6 shows the pressure distribution of fluid film considering only fluid inertia or both fluid inertia and cavitation at Re = 148.82. It can be seen from Figure 6a that due to the fluid inertia and side wall [7–9], there are significant pressure jumps at the inlet and outlet of texture, that is, the absolute values of the pressure gradients of these two regions are much larger than those of the other regions. Figure 6b shows that due to the fluid cavitation, the lower pressure at the inlet is greatly enhanced, and there is no change in the peak pressure. Figure 7 further illustrates the effect of fluid cavitation and Re on the pressure distribution of fluid film (where "I + C" is inertia and cavitation; "I" is only inertia, and "C" is only cavitation). It is worth noting that the fluid cavitation deceases the pressure jump at the inlet of the texture. The main reason is the decrease in fluid density in the cavitation region, where the fluid is a mixture of the liquid and vapor. It is well known that the mass is the only measure of inertia. As a result, a smaller fluid inertia causes a smaller pressure jump. In addition, with the increase in *Re*, the pressure in the low-pressure zone is gradually reduced. It is in accordance to experimental research papers on cavitation [1,33]; according to Braun et al. and Etsion et al., the greater the speed, the lower the pressure in the cavitation region. Moreover, it also can be found that the fluid cavitation improves the valley pressure value; however, the peak value is hardly affected.

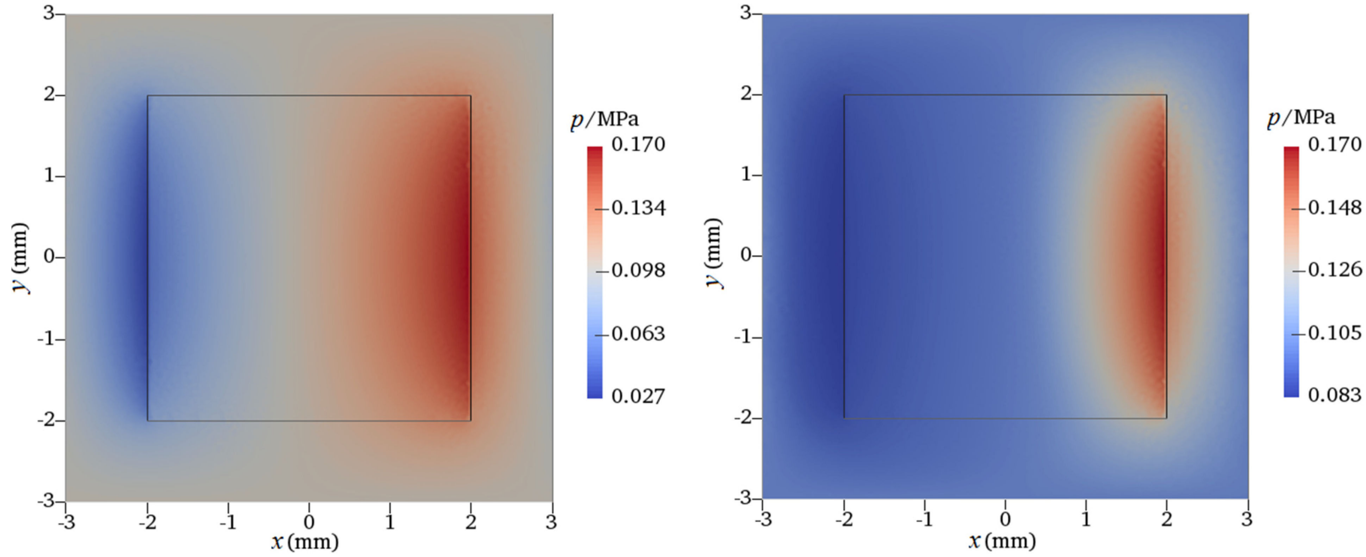

(**a**) Inertia effect (*Re* = 148.82) (**b**) Inertia and cavitation effect (*Re* = 148.82)

Figure 6. Pressure distribution comparison with and without cavitation.

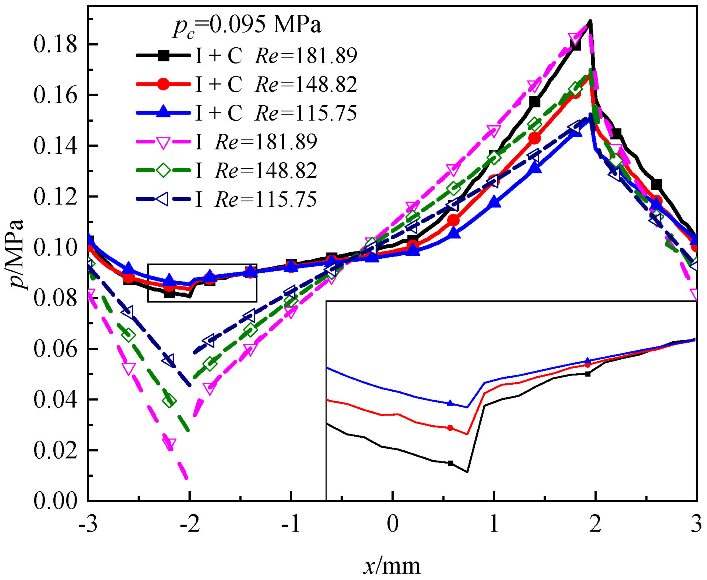

Figure 7. Effect of cavitation and *Re* on pressure distribution.

Figure 8 presents the effects of fluid inertia and *Re* on the pressure distribution. When the fluid inertia is not considered, with the increase in *Re*, the hydrodynamic effect is enhanced slowly, while the low-pressure zone caused by the fluid cavitation increases gradually. When the fluid inertia is considered, with the increase in *Re*, the hydrodynamic effect is rapidly enhanced. It shows that the fluid inertia significantly affects the local pressure distribution of fluid film. Compared with the results without the fluid inertia, when the *Re* is 115.75, 148.82, and 181.89 in turn, the incremental percentage Δp of the pressure peak is 18%, 28%, and 40%, respectively. When the fluid inertia is not considered, the peak pressure is much smaller. The greater the *Re*, the more serious the deviation is. At the same position of the longitudinal axis shown in Figure 8, the incremental percentage Δx of the high-pressure zone width is 133%, 161% and 196%, respectively. When the fluid inertia is not considered, the width of the high-pressure zone is greatly reduced; that is, the width of the low one is greatly increased. The greater the *Re*, the more obvious the change. The main reason is that the excessive expansion of the low-pressure zone caused by the fluid cavitation greatly weakens the hydrodynamic effect of texture.

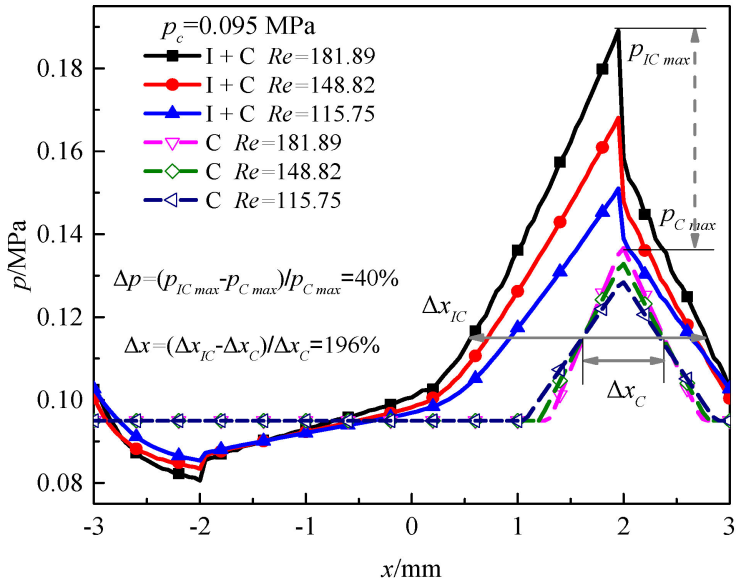

Figure 8. Effect of inertia and *Re* on pressure distribution.

Figure 9 shows the effect of *Re* on the LCC F_o; there are five cases: flat surface (Reynolds equation, RE-Flat); only texture (Reynolds equation, RE); texture and fluid cavitation (RE-JFO, C); texture and fluid inertia (present model only considering inertia, I); texture, fluid inertia and cavitation (present model considering both inertia and cavitation, I + C). When the fluid inertia is not considered, the LCCs of RE-Flat, RE and C are almost identical and unaffected by the *Re*. The main reason is that the pressure distribution is anti-symmetric for the case RE, and for the case C, although fluid cavitation avoids extremely small fluid pressure, it makes the high-pressure zone be reduced greatly. When the fluid inertia is only considered (I), with the increasing *Re*, the fluid inertia makes the pressure distribution of fluid film asymmetrical and then produces a small net LCC. This is consistent with many research papers on fluid inertia [7–9]. When both the fluid inertia and cavitation are considered, the fluid cavitation avoids extremely small fluid pressure, and the fluid inertia effectively enhances the hydrodynamic effect of texture and limits the excessive expansion of the low-pressure zone. As a result, a net LCC is generated, and it increases with the Increase in *Re*. When the *Re* value is 181.89, the net increment of the LCC is about 7.1% compared with the cases without fluid inertia. It is worth noting that the combined effect of fluid cavitation and inertia on the LCC is more significant than the case with only one of them. The main reason is the interaction between fluid inertia and cavitation, that is, their combined effect on the fluid pressure buildup.

4.3. Effect of p_c

Figure 10 presents the effect of cavitation pressure p_c on the fluid film pressure distribution for the case of Re = 165.35. For the current *Re* and gap thickness, the fluid inertia has a significant influence on the pressure distribution. It also be seen that the pressure jump at the inlet of the texture is far less than that of the texture outlet due to the smaller density of mixture at the inlet zone. For these two cases, with the increase in p_c, the pressure in the low-pressure zone increases rapidly. When the fluid inertia is not considered, with the increase in p_c, the low-pressure zone increases and the peak pressure decreases rapidly. The main reason is that the cavitation becomes more severe with the increasing p_c, and the excessive expansion of the low-pressure zone caused by the fluid cavitation greatly weakens the hydrodynamic effect of the texture. When the fluid inertia is considered, as the p_c increases, the low-pressure zone increases slowly. Another important finding is that the p_c has little effect on the pressure peak or the pressure jump at the texture outlet. As a result, when p_c is 0.065, 0.08, and 0.095, in turn, the incremental percentage Δp of the pressure peak with the fluid inertia is 10%, 15%, and 33%, respectively. At the same position of the longitudinal axis shown in Figure 10, the incremental percentage Δx of the high-pressure zone width is 13%, 29% and 149%, respectively. The main reason is that the fluid inertia significantly enhances the hydrodynamic effect of texture; thus, it greatly limits the excessive expansion of the low-pressure zone. The above analysis shows that the pressure jump at the texture outlet significantly affects the whole fluid film pressure buildup, and the one at the texture inlet mainly affects the local pressure distribution. According to the experimental results [34,35] of Sun et al., the pressure in the cavitation region is close to 0, and according to the experimental results [1,33] of Braun et al. and Etsion et al., it is near the atmospheric pressure. It indicates that the cavitation pressure is uncertain for actual working conditions. Therefore, for a working tribological component, the cavitation pressure can affect the fluid pressure buildup and LCC, especially when it has a larger value.

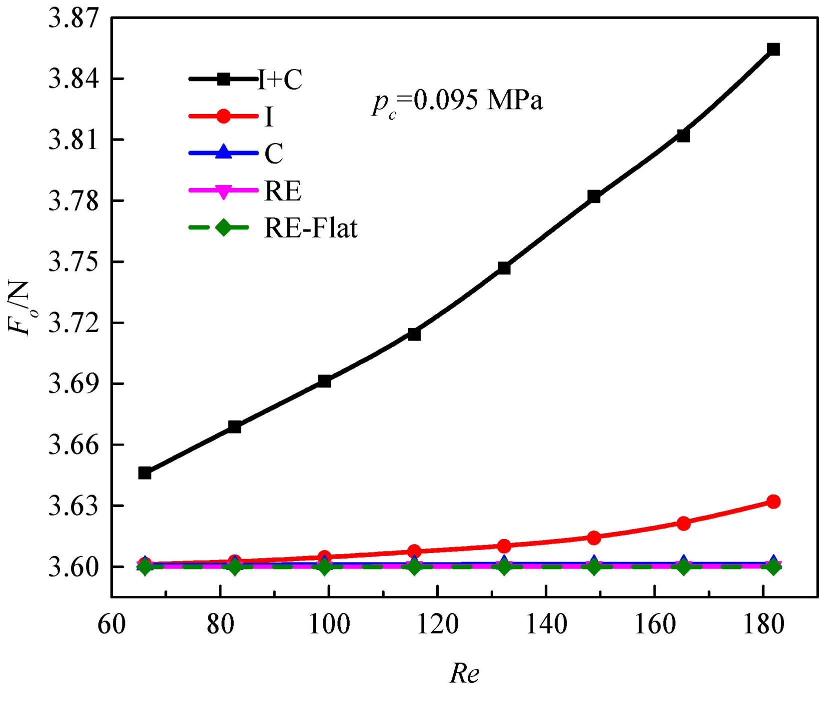

Figure 9. Effect of *Re* on F_o.

Figure 11 shows the effect of p_c on the LCC F_o. For these cases without the fluid cavitation (I, RE, RE-Flat), there is only one data point. When the fluid inertia is not considered (RE-Flat, RE, C), the LCC is almost fixed. Considering only the fluid inertia, the LCC has a small net increment. When both the fluid cavitation and inertia are considered, a considerable net increment of LCC is generated: the greater the p_c, the more significant the enhancement of LCC. When the p_c value is 0.095 (near the atmospheric pressure), the net increment of the LCC is about 6%. It is the contribution of the interaction of fluid cavitation and inertia; that is, the pressure in the low-pressure zone is significantly enhanced due to a larger p_c and the excessive expansion of the low-pressure zone is effectively limited due to the fluid inertia.

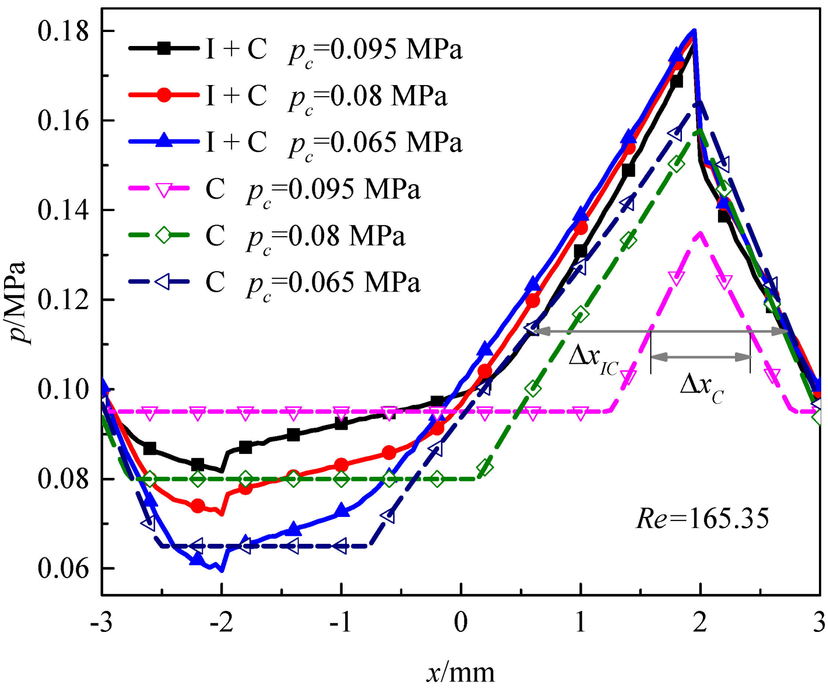

Figure 10. Effect of p_c on pressure distribution.

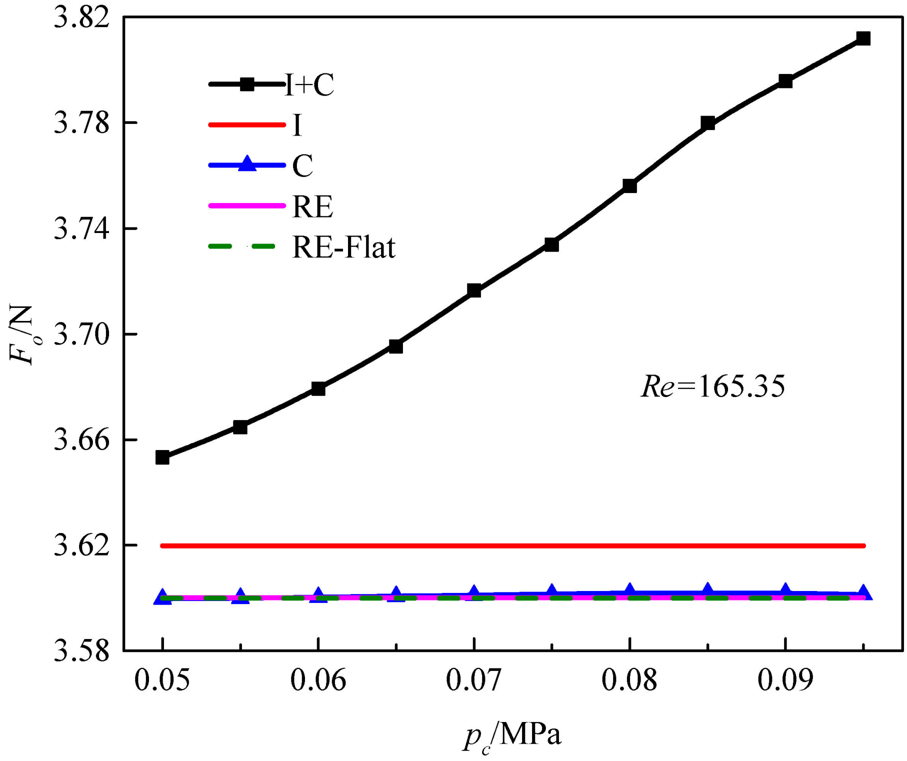

Figure 11. Effect of p_c on F_o.

4.4. Effect of S_r, h_1 and Shapes

Figure 12 shows the effects of texture area ratio S_r on the pressure distribution and LCC of the fluid film. The S_r value is a ratio of the texture area to the area of the upper surface cell, in which the texture area is adjusted by changing the texture size W_1. As shown in Figure 12a, with the increase in S_r, the hydrodynamic effect of the texture first increases and then decreases. The main reason is the location changes of the texture inlet and outlet.

It can be seen from Figure 12b that when the fluid inertia is not considered (RE, C), the S_r has little effect on the LCC. When the fluid inertia is only considered (I), the LCC increases slowly with the increase in S_r. When both the fluid cavitation and inertia are considered (I + C), the LCC increases firstly and then decreases with the increasing S_r, and when the S_r is about 0.44, the net increment of LCC is about 7.1%. Figure 13 shows the effect of texture depth h_1 on the pressure distribution and LCC of fluid film. As shown in Figure 13a, for the two cases, the hydrodynamic effect is gradually enhanced with the increase in h_1. It is worth noting that when the fluid inertia is not considered, the enhancement of hydrodynamic effect caused by the increase in h_1 is very weak. In addition, as the h_1 increases, the pressure jump generated by the fluid inertia becomes more significant. It is consistent with many studies [7–9] on the fluid inertia. The main reason is that the increase in h_1 enhances the effect of side walls. As shown in Figure 13b, it is also found that the h_1 value has the most significant effect on the LCC when both the fluid cavitation and inertia are considered. In the range of calculation, the maximum net increment of LCC is about 8%. Figure 14a–c show the effect of texture shape on the fluid film pressure distribution, where the texture shape includes a square, circle, and triangle, respectively. The pressure distributions of the square and the circle are similar, because they are symmetrical in the sliding direction. For the triangular shape, the pressure jump at the texture inlet is less than that at the outlet. The main reason is that the two side walls of the texture inlet are not perpendicular to the sliding direction. For these three shapes, the combined effect of fluid cavitation and inertia greatly enhances the hydrodynamic effect. As shown in Table 2, the combined effect has the most significant influence on the pressure buildup and LCC. Moreover, the square provides the maximum net LCC. The above analysis indicates that when only the fluid inertia or cavitation, or neither of them is considered, the enhancement of hydrodynamic effect is smaller and the contribution to LCC is very small or almost 0 for S_r, h_1 and recess shapes. Only when they are considered simultaneously can the adjustment of S_r, h_1 and recess shapes maximize the combined effect of fluid cavitation and inertia on the fluid pressure buildup and obtain the maximum LCC.

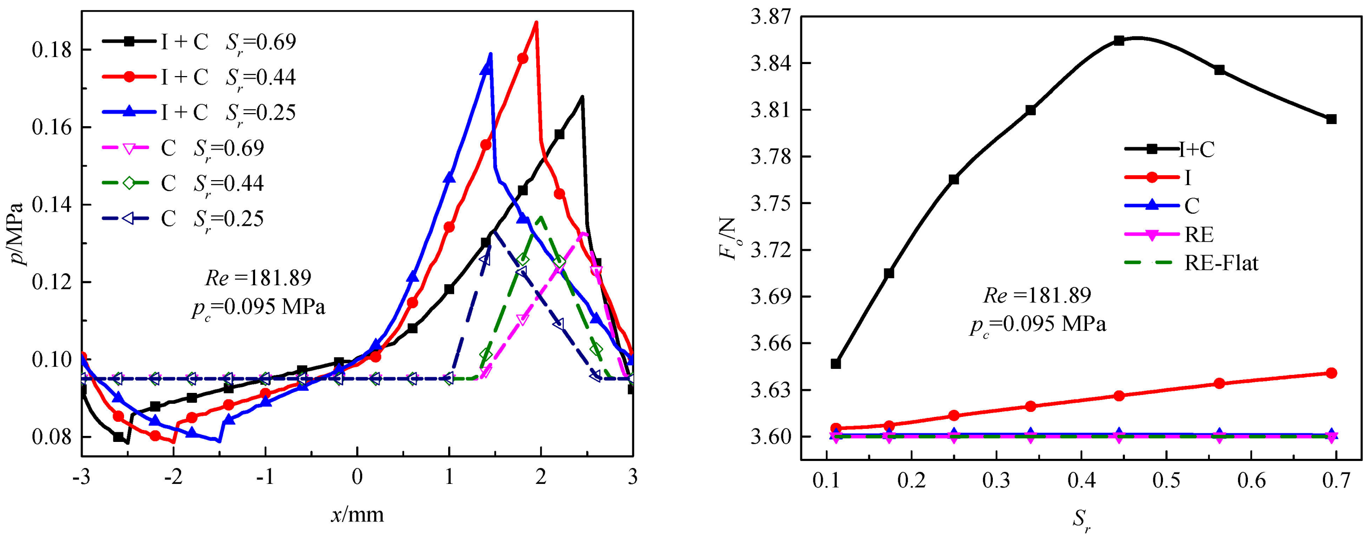

(**a**) Effect of S_r on pressure distribution (**b**) Effect of S_r on F_o

Figure 12. Effect of S_r.

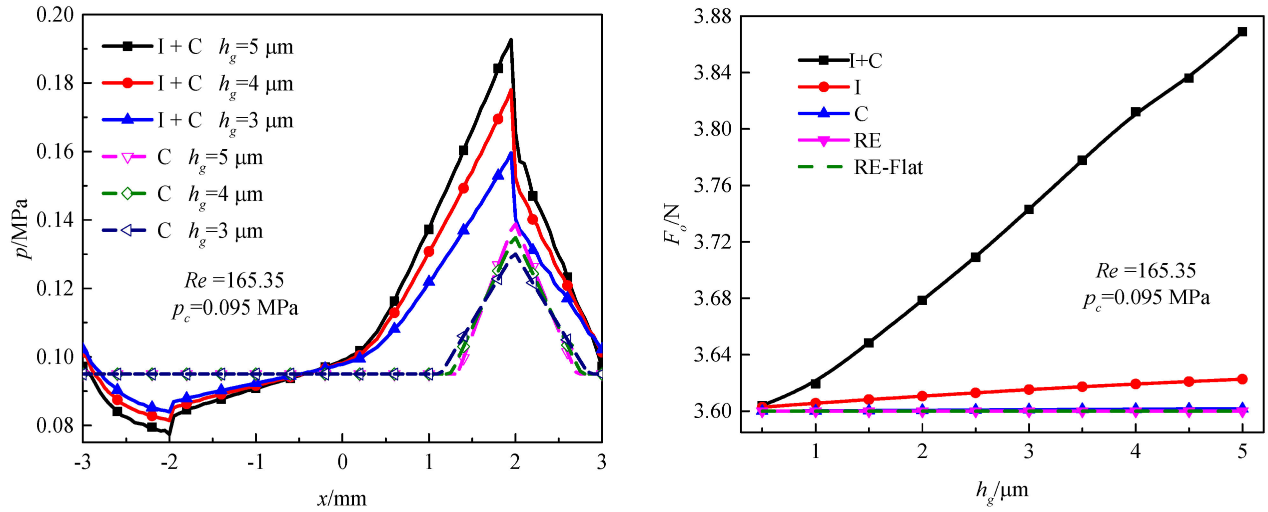

(**a**) Effect of h_1 on pressure distribution (**b**) Effect of h_1 on F_o

Figure 13. Effect of h_1.

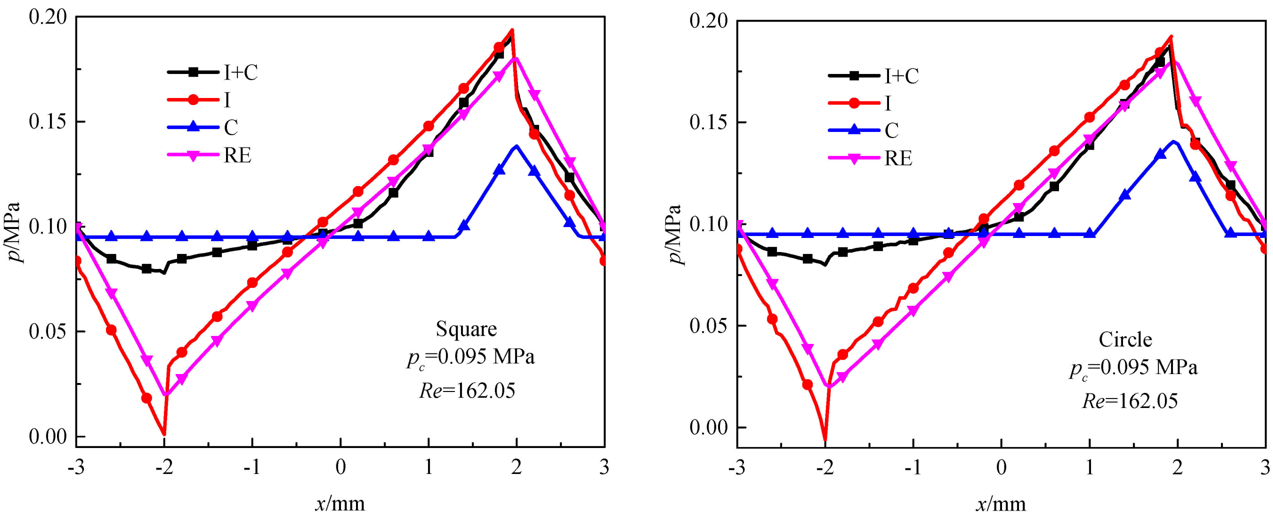

(**a**) Square recess (**b**) Circle recess

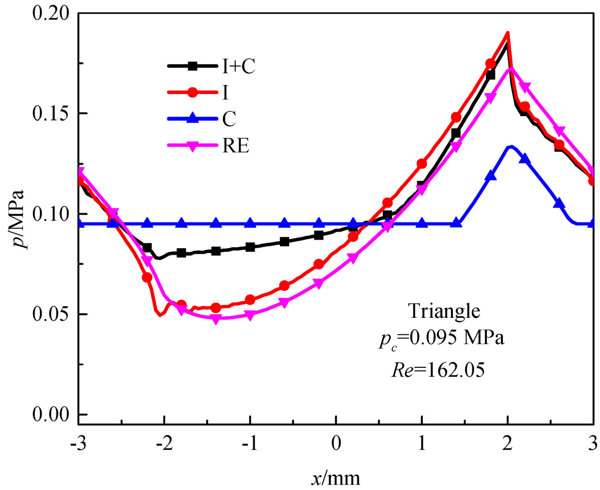

(**c**) Triangle recess

Figure 14. Effect of recess shapes on pressure distribution.

Table 2. Effect of recess shapes on peak pressure and LCC.

		Square	Circle	Triangle
Δp	$(p_{\max\,\mathrm{IC}} - p_{\max\,\mathrm{C}})/\,p_{\max\,\mathrm{C}}$	39.42%	38.88%	39.10%
	$(p_{\max\,\mathrm{I}} - p_{\max\,\mathrm{RE}})/\,p_{\max\,\mathrm{RE}}$	8.38%	8.94%	11.11%
LCC	IC	7.3%	7%	4.7%
	I	0.6%	0.43%	1.4%
	C	≈0	0.4%	≈0
	RE	≈0	≈0	≈0

5. Conclusions

A mathematical model with fluid cavitation and inertia was developed to investigate the fluid pressure buildup mechanism of parallel textured surfaces. The fluid cavitation was dealt with by the Rayleigh–Plesset model, and the fluid inertia was treated by an averaged method. The mass conservation equation, the momentum equations and the liquid volume fraction equation were solved with the finite element method. The Newton-downhill method was employed to solve the nonlinear equations. The numerical model was validated by comparing with the previously published experimental results and the numerical results by the RE-JFO and ANSYS FLUENT models. The combined effect of fluid cavitation and inertia on the fluid pressure buildup and LCC of hydrodynamic lubrication in parallel textured surfaces was analyzed and discussed.

Due to the fluid inertia and side wall, the pressure jumps occur at the texture inlet and outlet. The fluid cavitation significantly reduces the pressure jump at the texture inlet; thus, the fluid pressure distribution at the inlet is less affected by the fluid inertia.

The pressure jump at the outlet greatly increases the peak pressure and effectively limits the excessive extension of the low-pressure zone caused by the fluid cavitation, which greatly increases the width of the high-pressure zone and significantly enhances the hydrodynamic effect.

The fluid cavitation and inertia, especially their interaction, significantly affect the fluid film pressure buildup and generate a net LCC. The cavitation pressure can affect the fluid pressure buildup and LCC, especially when it has a larger value. The adjustment of recess area ratio S_r, recess depth h_1 and recess shapes can maximize the combined effect of fluid cavitation and inertia on the fluid pressure buildup and obtain the maximum LCC.

Funding: This research was funded by the National Natural Science foundation of China (No. 52005236), the Natural Science foundation of Gansu Province (No. 22JR5RA289), and the Hongliu Distinguished Young Talent Support Program of Lanzhou University of Technology (No. 02/062205).

Data Availability Statement: The data that support the findings of this study are available from the corresponding author upon reasonable request.

Conflicts of Interest: The author declares no conflict of interest.

Nomenclature

$\acute{R}_b$	Dynamic radius of cavitation bubbles, m
C_1, C_2	Empirical coefficient of vapor liquid transition
F_G, F_L	Vapor and liquid volume fraction per unit volume
F_o	Load-carrying capacity, N
h	Fluid film thickness, m
h_0, h_1	Gap thickness and square recess depth, m
I_{xx}, I_{xy}, I_{yy}	Flow characteristic parameters, m^3/s^2
l_x, l_y	Unit vectors in x and y directions
N	Number of initial bubbles per unit volume
p	Fluid film pressure, Pa
p_a, p_c	Ambient pressure and cavitation pressure, Pa
Q	Flow rate, m^3/s
q_x, q_y	Flow rates of unit length in x and y directions, m^2/s
R_b	Bubbles initial average radius, m
Re	Reynolds number, $Re = \rho_L u_0 h_0 / \mu_L$
S	Cavitation source term, $kg/(m^3{\cdot}s)$
T	Comprehensive coefficient
u	Velocity in x direction, m/s
u_0	Sliding velocity in x direction, m/s
v	Velocity in y direction, m/s
v_0	Sliding velocity in y direction, m/s
V_G, V_L	Vapor and liquid volume
w	Velocity in z direction, m/s
W_0, W_1	Slider and square recess length, m
x, y, z	Cartesian coordinate, m
λ_F, λ_{qp}	Downhill factors
μ, μ_G, μ_L	Mixture, vapor and liquid dynamic viscosity, Pa·s
ρ, ρ_G, ρ_L	Mixture, vapor and liquid density, kg/m^3

References

1. Braun, M.J.; Hannon, W.M. Cavitation formation and modelling for fluid film bearings: A review. *Proc. Inst. Mech. Eng. Part J J. Eng. Tribol.* **2010**, *224*, 839–863. [CrossRef]
2. Salant, R.F.; Homiller, S.J. Stiffness and leakage in spiral groove upstream pumping mechanical seals. *Tribol. Trans.* **1993**, *36*, 55–60. [CrossRef]
3. Etsion, I.; Burstein, L. A model for mechanical seals with regular microsurface structure. *Tribol. Trans.* **1996**, *39*, 677–683. [CrossRef]
4. Qiu, Y.Y.; Khonsari, M.M. Performance analysis of full-film textured surfaces with consideration of roughness effects. *J. Tribol.* **2011**, *133*, 021704. [CrossRef]
5. Ma, X.; Meng, X.; Wang, Y.; Peng, X. Suction effect of cavitation in the reverse-spiral-grooved mechanical face seals. *Tribol. Int.* **2019**, *132*, 142–153. [CrossRef]
6. Lin, Q.; Bao, Q.; Li, K.; Khonsari, M.M.; Zhao, H. An investigation into the transient behavior of journal bearing with surface texture based on fluid-structure interaction approach. *Tribol. Int.* **2018**, *118*, 246–255. [CrossRef]
7. Han, J.; Fang, L.; Sun, J.P.; Ge, S.R. Hydrodynamic lubrication of microdimple textured surface using three-dimensional CFD. *Tribol. Trans.* **2010**, *53*, 860–870. [CrossRef]
8. Han, J.; Fang, L.; Sun, J.P.; Wang, Y.Q.; Ge, S.R.; Zhu, H. Hydrodynamic lubrication of surfaces with asymmetric microdimple. *Tribol. Trans.* **2011**, *54*, 607–615. [CrossRef]
9. Ma, X.; Meng, X.; Wang, Y.; Liang, Y.; Peng, X. Fluid inertia effect on spiral-grooved mechanical face seals considering cavitation effects. *Tribol. Trans.* **2021**, *64*, 367–380. [CrossRef]
10. Ausas, R.; Ragot, P.; Leiva, J.; Jai, M.; Bayada, G.; Buscaglia, G.C. The impact of the cavitation model in the analysis of microtextured lubricated journal bearings. *J. Tribol.* **2007**, *129*, 868–875. [CrossRef]
11. Qiu, Y.Y.; Khonsari, M.M. On the prediction of cavitation in dimples using a mass-conservative algorithm. *J. Tribol.* **2009**, *131*, 041702. [CrossRef]
12. Zhang, J.Y.; Meng, Y.G. Direct observation of cavitation phenomenon and hydrodynamic lubrication analysis of textured surfaces. *Tribol. Lett.* **2012**, *46*, 147–158. [CrossRef]
13. Singhal, A.K.; Athavale, M.M.; Li, H.; Jiang, Y. Mathematical basis and validation of the full cavitation model. *J. Fluids Eng.* **2002**, *124*, 617–624. [CrossRef]
14. Bakir, F.; Rey, R.; Gerber, A.G.; Belamri, T.; Hutchinson, B. Numerical and experimental investigations of the cavitating behavior of an inducer. *Int. J. Rotating Mach.* **2004**, *10*, 15–25. [CrossRef]
15. Plesset, M.S. The dynamics of cavitation bubbles. *J. Appl. Mech.* **1949**, *16*, 277–282. [CrossRef]
16. Morris, N.J.; Shahmohamadi, H.; Rahmani, R.; Rahnejat, H.; Garner, C.P. Combined experimental and multiphase computational fluid dynamics analysis of surface textured journal bearings in mixed regime of lubrication. *Lubr. Sci.* **2018**, *30*, 161–173. [CrossRef]
17. Shahmohamadi, H.; Rahmani, R.; Rahnejat, H.; Garner, C.P.; Dowson, D. Big end bearing losses with thermal cavitation flow under cylinder deactivation. *Tribol. Lett.* **2015**, *57*, 2. [CrossRef]
18. Dhande, D.Y.; Pande, D.W. Multiphase flow analysis of hydrodynamic journal bearing using CFD coupled fluid structure interaction considering cavitation. *J. King Saud Univ.-Eng. Sci.* **2018**, *30*, 345–354. [CrossRef]
19. Cupillard, S.; Glavatskih, S.; Cervantes, M.J. Computational fluid dynamics analysis of a journal bearing with surface texturing. *Proc. Inst. Mech. Eng. Part J J. Eng. Tribol.* **2008**, *222*, 97–107. [CrossRef]
20. Mishra, S.; Choudhury, A.; Sahu, S. CFD investigation of influences of reverse textures on bearing surface of a journal bearing. *J. Appl. Fluid Mech.* **2014**, *7*, 395–399.
21. Song, Y.; Gu, C.W. Development and validation of a three-dimensional computational fluid dynamics analysis for journal bearings considering cavitation and conjugate heat transfer. *J. Eng. Gas Turbines Power* **2015**, *137*, 122502. [CrossRef]
22. Wang, T.; Huang, W.F.; Liu, Y.; Liu, X.F.; Wang, Y.M. A homogeneous phase change model for two-phase mechanical seals with three-dimensional face structures. *J. Tribol.* **2014**, *136*, 041708. [CrossRef]
23. Constantinescu, V.N.; Galetuse, S. Operating characteristics of journal bearings in turbulent inertial flow. *J. Lubr. Technol.* **1982**, *104*, 173–179. [CrossRef]
24. Brunetière, N.; Tournerie, B. Finite element solution of inertia influenced flow in thin fluid films. *J. Tribol.* **2007**, *129*, 876–886. [CrossRef]
25. Wang, T.; Huang, W.F.; Liu, X.F.; Li, Y.J.; Wang, Y.M. Experimental study of two-phase mechanical face seals with laser surface texturing. *Tribol. Int.* **2014**, *72*, 90–97. [CrossRef]
26. Li, W.; Stephens, L.S.; Wenk, J.F. Experimental benchmarking of the numerical model of a radial lip seal with a surface textured shaft. *Tribol. Trans.* **2013**, *56*, 75–87. [CrossRef]
27. Rao, T.V.V.L.N.; Rani, A.M.A.; Nagarajan, T.; Hashim, F.M. Analysis of slider and journal bearing using partially textured slip surface. *Tribol. Int.* **2012**, *56*, 121–128. [CrossRef]
28. Cross, A.T.; Sadeghi, F.; Rateick, G.R.; Rowan, S.; Laboda, D. Temperature distribution in pocketed thrust washers. *Tribol. Trans.* **2015**, *58*, 31–43. [CrossRef]
29. Tomanik, E. Modelling the hydrodynamic support of cylinder bore and piston rings with laser textured surfaces. *Tribol. Int.* **2013**, *59*, 90–96. [CrossRef]
30. Morgut, M.; Nobile, E.; Bilus, I. Comparison of mass transfer models for the numerical prediction of sheet cavitation around a hydrofoil. *Int. J. Multiph. Flow* **2011**, *37*, 620–626. [CrossRef]

31. Jakobsson, B.; Floberg, L. *The Finite Journal Bearing, Considering Vaporization*; Chalmers Tekniska Högskolas Handlingar: Gothenburg, Sweden, 1957.
32. Meng, X.K.; Bai, S.X.; Peng, X.D. Lubrication film flow control by oriented dimples for liquid lubricated mechanical seals. *Tribol. Int.* **2014**, *77*, 132–141. [CrossRef]
33. Etsion, I.; Ludwig, L.P. Observation of pressure variation in the cavitation region of submerged journal bearings. *ASME J. Lubr. Tech.* **1982**, *104*, 157–163. [CrossRef]
34. Sun, D.C.; Brewe, D.E. A high-speed photography study of cavitation in a dynamically loaded journal bearing. *ASME J. Tribol.* **1991**, *113*, 287–292. [CrossRef]
35. Sun, D.C.; Brewe, D.E.; Abel, P.B. Simultaneous pressure measurement and high-speed photography study of cavitation in a dynamically loaded journal bearing. *ASME J. Tribol.* **1993**, *115*, 88–95. [CrossRef]